# Prediction of Common Mode Far-Field Radiation for a Low-Side Buck Converter With Cables via Feko Electromagnetic Simulation

Weixin Wang, Junping He, *Senior Member, IEEE*, Junhua Shu, Han Wang, and Lingling Cao

***Abstract*—The electromagnetic radiation emitted from the power converter is readily capable of inducing failure of the electromagnetic compatibility certification. The development of an accurate and reliable radiation model, as well as a prediction method, could be effectively beneficial in resolving these challenges. This article examines the equivalent driving sources and the electromagnetic prediction of the common mode (CM) radiation of a low-side Buck converter with cables. Based on the crucial concept of CM voltage mutation, two distinct types of CM driving sources in such a Buck converter are examined: the same-direction sources and the opposite-direction sources. The radiation transfer functions for various types of driving sources are then obtained using three-dimensional modeling with an electromagnetic simulation tool, and then the far-field CM radiation is methodically evaluated via the superposition principle. Finally, a 30-MHz low-side Buck prototype with shielded cables is appropriately fabricated and tested, two suppression schemes are methodically suggested and verified, and the influence of the cable and printed circuit board size on the transfer functions is discussed in simulation. The proposed electromagnetic radiation mechanism, prediction method, and suppression schemes are anticipated to be of excellent significance in the analysis and optimization design of CM radiation in dc/dc converters.**

***Index Terms*—Common mode (CM) voltage mutation, electromagnetic simulation, far-field electromagnetic radiation, low-side buck converter, radiation mechanism.**

## I. Introduction

IT IS well known that a power converter easily generates strong electromagnetic radiation due to its fast-switching operation, which often causes the failure of electromagnetic compatibility (EMC) certification or unexpected delays in product development [1], [2]. Researchers have conducted a lot of research work on this EMC issue, such as the formation mechanisms, prediction approaches, and suppression techniques of electromagnetic radiation of power converters [3], [4], [5]. However, far-field radiation in nature is unintentional electromagnetic radiation, and its driving sources and radiator characteristics are completely hidden and complex. The large number, size, and densely packed passive/active components installed in power converters further increase the complexity of analyzing the radiation mechanisms [6]. Even worse, with the fast application of wide-bandgap semiconductor switches in power converters in recent years, their switching speed, which is on the order of nanoseconds (ns) tends to generate stronger electromagnetic noise compared with the traditional silicon switches [7], [8]. This brings more stringent EMC challenges to power electronics researchers and designers, who urgently need to be thoroughly examined and solved.

Up till now, researchers from all over the world have investigated the mechanism of electromagnetic radiated emission (RE) and reported that common mode (CM) currents on cables are the main cause of electrical or electronic products exceeding the RE standard below a few hundred MHz [9], [10], [11], [12], [13], [14], [15], [16]. The equivalent voltage/current driven source method and the imbalance difference method are two popular methodologies for examining unintentional CM radiation sources and radiators in electronic products [9], [10], [11], [12], [13], [14]. Unfortunately, for products such as switched-mode power supplies (SMPS), there are many active or passive components among the power cables, which makes it difficult to utilize the above-mentioned methods. Yao et al. [15], [16] proposed the equivalent antenna impedance approach to predict the far-field radiation of Flyback power supplies and a nonisolated Buck converter. However, the proposed approach was difficult to handle scenarios with multiple CM driving sources or complex layout cables. He et al. proposed the concept of generalized CM potential (GCMP) to identify the longitudinal CM voltage mutation and carefully examined the equivalent CM driving mechanisms and parasitic radiator's analytical calculations for a Buck and a Boost converter [17], [18]. This methodology could effectively identify multiple CM radiation driving sources, but these investigations employed approximate antenna structures and analytical formulas, which could readily lead to errors. In particular, the aforementioned radiator's analytical method is difficult to apply to main circuits or power cables with complex structures, and its calculation process was also cumbersome, which thereby cannot be recommended for power supply designers. Fortunately, commercial electromagnetic simulation

Received 11 February 2025; revised 7 April 2025; accepted 4 May 2025. Date of publication 9 May 2025; date of current version 30 June 2025. This work was supported in part by the National Natural Science Foundation of China under Grant 52077046 and in part by Shenzhen Science and Technology Plan under Grant JSGG20201201100406017. Recommended for publication by Associate Editor S. Kumar Mazumder. *(Corresponding author: Junping He.)*

The authors are with the Harbin Institute of Technology Shenzhen, Shenzhen 518055, China (e-mail: hejunping@hit.edu.cn).

Color versions of one or more figures in this article are available at https://doi.org/10.1109/TPEL.2025.3568354.

Digital Object Identifier 10.1109/TPEL.2025.3568354

software has now been vastly developed, and physical modeling and far-field calculation methods of complex radiators have also matured. Therefore, this article aims to combine the GCMP method with electromagnetic simulation tools for the first time to explore the accurate mechanism model and quantitative prediction method of far-field radiation in SMPS. Specifically, this study identifies several radiation driving sources for a very high frequency (VHF) low-side Buck converter with shielded cables, adopts the Feko electromagnetic software to precisely model and quantify the radiation characteristics of the multisegment radiator structure, and ultimately achieves precise prediction, characteristic analysis, and suppression design of the converter's far-field radiation.

The rest of this article is organized as follows. First, based on the GCMP concept, the same-direction voltage driving mode and the opposite-direction voltage driving mode for cables with two CM voltage mutations are methodically introduced. In Section II, the preliminary prediction methodologies for the CM far-field radiation of the cables are proposed. Then, a low-side Buck converter with shielded cables is introduced in Section III, and the equivalent CM driving sources of the main circuit are analyzed and decomposed using the method proposed in the former section. In addition, for complex radiators with multiple driving sources, the Feko electromagnetic software is utilized for 3-D modeling, and the far-field radiation transfer functions of various submodes are calculated in Section IV. Thereafter, the far-field radiation prediction, radiation characteristics, and two suppression schemes of the low-side Buck converter are verified in some detail within Section V. Finally, the effects of dimension changes of the main circuit and cable on the radiation propagation are appropriately simulated and discussed. The methodologies and results of this article are anticipated to have very good significance for the analysis, prediction, and improvement of far-field REs encountered by power electronic converters.

## II. Cables With Multiple Equivalent CM Driving Sources and the Far-Field Radiation Formulas

The CM voltage mutation methodology could readily identify the equivalent CM driving source in cables. This section first briefly reviews this approach, then investigates the CM voltage mutation phenomena when there are multiple active or passive components among cables, and proposes prediction formulas for the CM far-field radiation of cables with multiple driving sources.

### A. Equivalent CM Driving Source Produced by CM Voltage Mutation

Recent studies and experiments have revealed that CM voltage mutations on cables or components are the equivalent driving sources with clear physical meanings for the formation of CM currents [10], [15]. It is convenient to identify various CM voltage mutation phenomena in cables or circuits via the GCMP concept, and the key viewpoints of this approach can be summarized as follows.

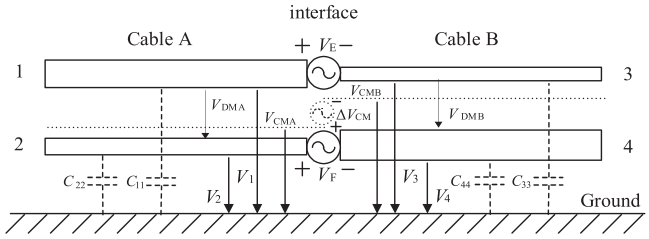


Fig. 1. CM voltage mutation between two transmission lines.

In Fig. 1, the left cable A and the right cable B are connected through two voltage sources $V_E$ and $V_F$. The cable A is composed of conductors 1 and 2, and the cable B is composed of conductors 3 and 4. $V_E$ or $V_F$ can represent the voltage on small-scale active or passive devices at the interface. Based on the principle of equal total charge to ground [15], the generalized CM voltage of the left cable and the right cable, which are, respectively, denoted by $V_{\mathrm{CMA}}$ and $V_{\mathrm{CMB}}$, can be expressed by (1) and (2)

$$V_{\mathrm{CMA}} = \frac{C_{11}}{C_{11}+C_{22}}V_1+\frac{C_{22}}{C_{11}+C_{22}}V_2 = k_1V_1 + (1-k_1)V_2 \tag{1}$$

$$V_{\mathrm{CMB}} = \frac{C_{33}}{C_{33}+C_{44}}V_3+\frac{C_{44}}{C_{33}+C_{44}}V_4 = k_3V_3 + (1-k_3)V_4 \tag{2}$$

where the coefficients $k_1$ and $k_3$ are simplified representations of the capacitance relationship, i.e., the asymmetry coefficients as displayed in [10]. In addition, $V_i$ denotes the voltage of the $i$th conductor with respect to ground, $C_{\mathrm{ii}}$ represents the self-capacitance unit length of the $i$th conductor, and the numerator factor $i$ signifies the serial number of the conductor.

A sudden CM voltage change will happen at the interface, i.e., CM voltage mutation $\Delta V_{\mathrm{CM}}$ in (3), and it is also shown by the dashed voltage source symbol in the middle of Fig. 1. $V_{\mathrm{DMA}}$ and $V_{\mathrm{DMB}}$ in (3) denote the differential mode (DM) voltages of cable A and cable B, respectively. The voltage mutation is determined by the conductor structure parameters and the voltage in DM channels only, so it can be treated as an independent equivalent driving source in CM channels

$$\Delta V_{\mathrm{CM}} = V_{\mathrm{CMA}} - V_{\mathrm{CMB}} = k_1V_E + (1-k_1)V_F + (k_1-k_3)V_{\mathrm{DMB}}. \tag{3}$$

There are two type causes for the CM voltage mutation occurring at the interface. The first is that the longitudinal voltage sources between the cables can become a CM voltage driving source, i.e., the expression $k_1V_E$+(1-$k_1$)$V_F$. The second is that the transverse DM voltage between the conductors can also become a CM voltage driving source as the cross-section of the two cables alters, i.e., the term "($k_1$-$k_3$)$V_{\mathrm{DMB}}$" in (3).

This equivalent CM voltage driving source, $\Delta V_{\mathrm{CM}}$ is capable of driving the left cable and the right cable to form a parasitic radiator and produce CM far-field radiation [10], [13], [14], [15].

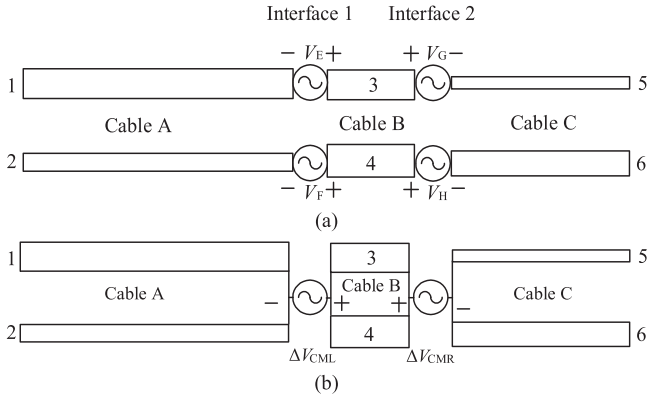


Fig. 2. Cables with two CM voltage mutation sources. (a) Cables structure. (b) Simplified CM driving sources and cables.

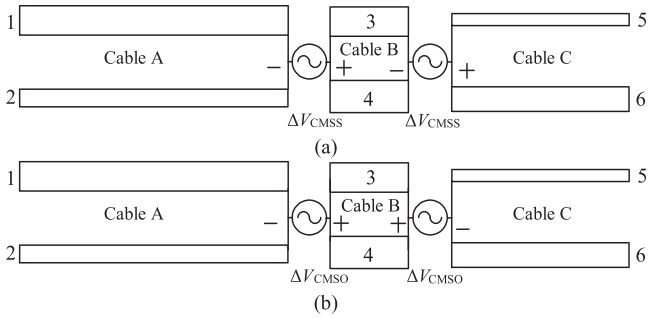


Fig. 3. Decomposition of two CM voltage mutation sources. (a) Dual-subdriving-same-direction sources mode. (b) Dual-subdriving-opposite-direction sources mode.

### B. Cables With Two CM Driving Sources and Their Radiation Predictions

For a piece of electrical or electronic equipment, multiple CM voltage mutations often occur between input and output cables [13]. This section takes three cables with two CM voltage mutations as an example to introduce the CM radiation prediction method.

*1). Two CM Driving Sources and Radiation Prediction:* Fig. 2(a) illustrates three cables with two CM voltage mutation interfaces among them. Setting the left side CM voltage mutation as $\Delta V_{\mathrm{CML}}$ and the right side one as $\Delta V_{\mathrm{CMR}}$, then these CM voltage mutations will act as the CM driving sources. Furthermore, the above three cables with voltage sources can be redrawn as Fig. 2(b) [18]. It can be easily understood that this is a complex radiation structure with multiple driving sources and multiple conductors.

According to the superposition theorem of a linear system, the total radiation of these radiators with multiple driving sources can be considered as the superposition of the radiation produced by every individual driving source. To this end, the transfer function of the radiators is set as $\boldsymbol{T}_{\Delta\mathrm{VCML}}$ when $\Delta V_{\mathrm{CML}}$ acts alone, and the transfer function is taken as $\boldsymbol{T}_{\Delta\mathrm{VCMR}}$ when $\Delta V_{\mathrm{CMR}}$ acts alone; then, the total radiation $\boldsymbol{E}_{\mathrm{total}}$ can be calculated via the following equation:

$$\boldsymbol{E}_{\mathrm{total}}(r,\varphi,h) = \Delta V_{\mathrm{CML}}\boldsymbol{T}_{\Delta\mathrm{VCML}}(r,\varphi,h) + \Delta V_{\mathrm{CMR}}\boldsymbol{T}_{\Delta\mathrm{VCMR}}(r,\varphi,h) \quad (4)$$

where $r$, $\varphi$, and $h$ represent the cylindrical coordinates of the observation point. Equation (4) also means that as long as the driving sources and transfer functions are specified, the radiation intensity can be rationally predicted.

*2). Two Type CM Subdriving Sources and Their Radiation Prediction Method:* Furthermore, the two CM driving sources of Fig. 2(b) can be decomposed into a dual-sub-driving source model with the same direction and magnitude, as illustrated in Fig. 3(a), and a dual-subdriving source model with the same magnitude but opposite direction, as demonstrated in Fig. 3(b). The values of the subdriving sources, namely $\Delta V_{\mathrm{CMSS}}$ and $\Delta V_{\mathrm{CMSO}}$, can be evaluated via (5) and (6), respectively, [18]

$$\Delta V_{\mathrm{CMSS}} = (\Delta V_{\mathrm{CML}} - \Delta V_{\mathrm{CMR}})/2 \quad (5)$$

$$\Delta V_{\mathrm{CMSO}} = (\Delta V_{\mathrm{CML}} + \Delta V_{\mathrm{CMR}})/2. \quad (6)$$

Similarly, the far-field radiation generated by $\Delta V_{\mathrm{CML}}$ and $\Delta V_{\mathrm{CMR}}$ in Fig. 2(b) can also be considered as the sum of the far-field radiation generated by the $\Delta V_{\mathrm{CMSS}}$ and $\Delta V_{\mathrm{CMSO}}$, respectively, as illustrated in Fig. 3(a) and (b). The following equation is able to clearly represent the above-mentioned relationship:

$$\boldsymbol{E}_{\mathrm{total}}(r,\varphi,h) = \Delta V_{\mathrm{CMSS}}\boldsymbol{T}_{\Delta\mathrm{VCMSS}}(r,\varphi,h) + \Delta V_{\mathrm{CMSO}}\boldsymbol{T}_{\Delta\mathrm{VCMSO}}(r,\varphi,h) \quad (7)$$

where $\boldsymbol{T}_{\Delta\mathrm{VCMSS}}$ denotes the radiator transfer function when $\Delta V_{\mathrm{CMSS}}$ acts alone, and $\boldsymbol{T}_{\Delta\mathrm{VCMSO}}$ represents the radiator transfer function when $\Delta V_{\mathrm{CMSO}}$ acts alone.

By the way, the proposed subdriving source models in Fig. 3 possess fairly clear mathematical definitions and physical meanings in fact. In particular, when the size of cable B is relatively small, $\Delta V_{\mathrm{CMSS}}\boldsymbol{T}_{\Delta\mathrm{VCMSS}}$ represents the radiation driving source between cable A and cable C, and its role. In addition, $\Delta V_{\mathrm{CMSO}}\boldsymbol{T}_{\Delta\mathrm{VCMSO}}$ represents the radiation driving source from cable B to cable C and cable A, and its role. In Section III, a low-side Buck converter with cables is taken as a typical example for detailed analysis and application.

## III. Far-Field Radiation Mechanism Model of a Low-Side Buck Converter With Cables

The low-side Buck converter is a common nonisolated power supply and is often utilized in the field of power semiconductor switching characteristic tests and LED lighting, etc. This section investigates the CM radiation mechanism and model of the low-side Buck converter with horizontal cables using the proposed CM voltage mutation and dual-driving-source approach.

### A. Low-side Buck Converter With Cables and its CM Radiation Analysis

Except for the switch on the negative bus, the function of a low-side Buck converter is similar to a normal Buck converter.

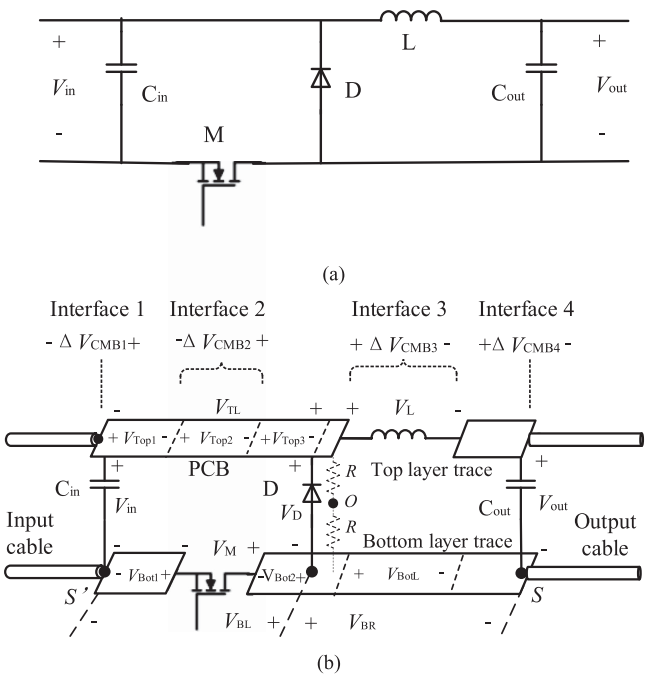


Fig. 4. Low-side Buck converter and its main structure. (a) Main circuit. (b) Main geometrical structure of the converter.

The CM driving sources of the low-side Buck can be readily identified and quantified via the preceding CM voltage mutation approach.

Fig. 4(a) illustrates the circuit topology of a low-side Buck converter, and Fig. 4(b) demonstrates the main geometrical structure of the studied low-side Buck converter with horizontal input and output cables. For the convenience of analysis and experiment, the size of the active and passive components in this converter is set smaller than that of the printed circuit board (PCB) trace of the main circuit. The cross-sectional area of the PCB traces also remains generally constant and straight. As a result, the dominant electromagnetic field between the PCB traces would chiefly be the quasi-transverse electromagnetic mode (QTEM). The inductor $L$ and the semiconductor switch $M$ can be viewed as longitudinal voltage sources due to their small geometric dimensions.

Fig. 4(b) also presents the meaning and positive direction of each voltage symbol. According to the CM voltage mutation analysis in Section II-A, this Buck converter possesses four CM voltage mutations at interface 1 to interface 4 in total, namely $\Delta V_{\mathrm{CMB1}}$ to $\Delta V_{\mathrm{CMB4}}$, as illustrated at the top of Fig. 4(b). These are the interface between the input cable and the PCB traces, the two terminals of the switch $M$, the two terminals of the inductor $L$, and the interface between the PCB traces and the output cable.

The values of these four CM voltage mutations can be evaluated as follows:

$$\Delta V_{\mathrm{CMB1}} = (k_{\mathrm{PCB}} - k_{\mathrm{incab}})V_{\mathrm{in}} \tag{8}$$

$$\Delta V_{\mathrm{CMB2}} = k_{\mathrm{PCB}}V_M - (1 - k_{PCB})V_{\mathrm{Top2}} \tag{9}$$

$$\Delta V_{\mathrm{CMB3}} = k_{\mathrm{PCB}}V_L + (1 - k_{\mathrm{PCB}})V_{\mathrm{BotL}} \tag{10}$$

$$\Delta V_{\mathrm{CMB4}} = (k_{\mathrm{PCB}} - k_{\mathrm{outcab}})V_{\mathrm{out}} \tag{11}$$

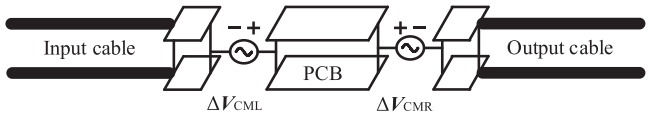


Fig. 5. Simplified two equivalent CM driving sources model of the low-side Buck converter with input and output cables.

in which $k_{\mathrm{incab}}$, $k_{\mathrm{PCB}}$, and $k_{\mathrm{outcab}}$ in order represent the asymmetry factors of the input cable, the PCB traces, and the output cable; $V_{\mathrm{in}}$ and $V_{\mathrm{out}}$ denote the input voltage and output voltage of the converter, respectively; $V_M$ and $V_L$ in order signify the voltage crossing the semiconductor switch and the inductor; and finally, $V_{\mathrm{Top2}}$ and $V_{\mathrm{BotL}}$ represent the voltage drop of the PCB trace just above the switch and under the inductor, respectively.

Under the driving of the CM voltage mutations mentioned above, this Buck converter and its cables generate CM current and electromagnetic radiation. The number of four driving voltage sources listed above is still relatively large, and if each driving source is considered separately, the radiation treatment will be time-consuming. Since $\Delta V_{\mathrm{CMB1}}$ is very small because the $V_{\mathrm{in}}$ ripple is generally small and the two driving sources on the left side are very close in space, $\Delta V_{\mathrm{CMB1}}$ and $\Delta V_{\mathrm{CMB2}}$ can be rationally merged into one source to simplify the processing, namely $\Delta V_{\mathrm{CML}}$. Similarly, the two driving sources on the right side, $\Delta V_{\mathrm{CMB3}}$ and $\Delta V_{\mathrm{CMB4}}$, can be merged into one source, $\Delta V_{\mathrm{CMR}}$. Then a simplified CM model with two driving sources of the low-side Buck converter can be obtained in the following form as Fig. 5:

$$\Delta V_{\mathrm{CML}} = \Delta V_{\mathrm{CMB1}} + \Delta V_{\mathrm{CMB2}} \tag{12}$$

$$\Delta V_{\mathrm{CMR}} = \Delta V_{\mathrm{CMB3}} + \Delta V_{\mathrm{CMB4}}. \tag{13}$$

It can be observed that the CM model presented in Fig. 5 is almost identical to that demonstrated in Fig. 2(b); therefore, (7) can be applied to CM radiation prediction of the low-side Buck converter with horizontal cables.

### *B. CM Radiation Model of the Low-Side Buck Converter With Shielded Cables*

Fig. 6 demonstrates the overall layout and detailed structure of the low-side Buck converter with horizontal shielded input and output cables in the present investigation. Several special designs are adopted here to avoid the effects of DM radiation. For example, shielded input and output cables are utilized to eliminate their DM radiation. The input battery and load resistor are commonly designed with the same diameter as the cables and are also shielded. The small $M$-switch driver circuit is shielded by a metal shell. Therefore, the radiation structure of Fig. 6 is mainly CM in nature, and its CM far-field radiation can be calculated via the formulas in Section II after determining the CM driving sources and radiation transfer functions.

*1). CM Driving Source $\Delta V_{CML}$ and $\Delta V_{CMR}$ and Their Measurement:* The main CM driving voltages of the low-side Buck converter ($\Delta V_{\mathrm{CML}}$ and $\Delta V_{\mathrm{CMR}}$) can be readily determined in fact, and their derivation details are explained below. Since

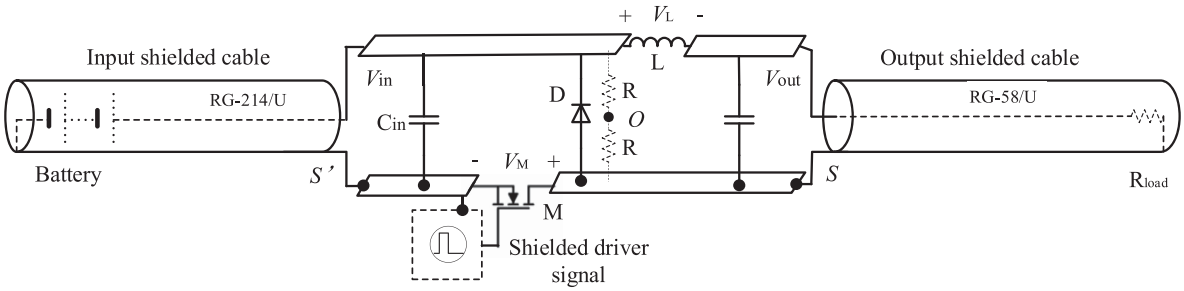


Fig. 6. Overall structure of the low-side Buck converter and its horizontal shielded cables.

the shielded cable is utilized for the input and output parts, $k_{\text{incab}}$ and $k_{\text{outcab}}$ would be reasonably equal to zero. The PCB trace width of the top and bottom layers is the same here, so $k_{\text{PCB}}$ is rationally equal to or very close to 0.5. According to the definition of the CM voltage $\Delta V_{\text{CML}}$, it is evaluated as $V_{\text{in}}/2+(V_M - V_{\text{Top2}})/2$, and coincidentally, this voltage can be simplified to $V_{\text{os}'}$ according to the following equation:

$$\begin{aligned}\Delta V_{\text{CML}} &= V_{\text{in}}/2 + (V_M - V_{\text{TOP2}})/2 \\ &= (V_D + V_{\text{Bot1}} + V_M + V_{\text{Bot2}} + V_{\text{Top1}} + V_{\text{Top2}} \\ &\quad + V_{\text{Top3}} + V_M - V_{\text{Top2}})/2 \\ &= V_D/2 + V_{\text{Bot1}} + V_M + V_{\text{Bot2}} \\ &= V_{\text{OS}'}. \end{aligned} \tag{14}$$

In this relation, the value of $V_{\text{Topi}}$ is almost equal to the value of $V_{\text{Boti}}$ below it, because the widths of the upper- and lower-layer PCB traces are the same, that is, the impedance and the working current through them are almost the same. Therefore, it can be finally found that $\Delta V_{\text{CML}}$ is equal to the voltage $V_{\text{os}'}$, which is just the voltage between the midpoint $O$ of the diode $D$ and the outer skin point $S$' of the input coaxial cable. This $O$ point can be made by connecting two series resistors $R$ with appropriate resistance to the diode $D$ in parallel. That is, the $V_{\text{os}'}$ can be measured directly, as demonstrated in Figs. 4(b) and 6.

Similarly, $\Delta V_{\text{CMR}}$ can also be determined as $V_{\text{os}}$ based on (15), and it can be measured by the voltage between point $O$ and the outer skin point $S$ of the output coaxial cable, as illustrated in Figs. 4(b) and 6

$$\Delta V_{\text{CMR}} = (V_{\text{out}} + V_L + V_{\text{BotL}})/2 = V_D/2 + V_{\text{BR}} = V_{\text{OS}}. \tag{15}$$

*2). CM Driving Source $\Delta V_{CMSS}$ and $\Delta V_{CMSO}$ and Their Physical Meanings:* Utilizing the measured $\Delta V_{\text{CML}}$ or $\Delta V_{\text{CMR}}$ voltage, the decomposed CM subdriving voltage sources ($\Delta V_{\text{CMSS}}$ and $\Delta V_{\text{CMSO}}$) can be calculated with the given details as follows:

$$2\Delta V_{\text{CMSS}} = \Delta V_{\text{CML}} - \Delta V_{\text{CMR}} = V_{\text{os}'} - V_{\text{os}} = V_{\text{ss}'} \tag{16}$$

$$\Delta V_{\text{CMSO}} = (\Delta V_{\text{CML}} + \Delta V_{\text{CMR}})/2 = (V_{\text{in}} + V_{\text{TL}} + V_{\text{BR}})/2. \tag{17}$$

It can be seen that $\Delta V_{\text{CMSS}}$ and $\Delta V_{\text{CMSO}}$ of the radiation model have clear physical meanings as mentioned in Section II-B2. For example, $2\Delta V_{\text{CMSS}}$, that is, $V_{\text{SS}'}$, represents the longitudinal CM voltage difference between the input and output cables, which is also close to the $V_M$ of the M-switch. In addition, $\Delta V_{\text{CMSO}}$ can be determined by the input voltage $V_{\text{in}}$, the voltage drop $V_{\text{TL}}$ on the upper-left PCB, and the voltage drop $V_{\text{BR}}$ on the lower-right PCB. Due to the closeness of $V_{\text{in}}$ to dc, $\Delta V_{\text{CMSO}}$ can be reasonably determined by the latter two, representing the transverse voltage from the main circuit of the low-side Buck converter to the shielded cables. The abovementioned features can be directly utilized for the RE analysis, prediction, and suppression design of this power converter.

### C. Total Far-Field Radiation Formula for Horizontal Cables With Two Subdriving Sources

When the input cable, output cable, and converter are horizontally laid out above the ground plane during RE testing, the CM far-field radiation essentially remains the horizontal component. Under such a circumstance, the total horizontal CM radiation intensity of the cables would be the sum of the field intensity formed by the same-direction driving sources $\Delta V_{\text{CMSS}}$ and the opposite-direction driving sources $\Delta V_{\text{CMSO}}$, and the calculation expression is given by

$$\begin{aligned}\boldsymbol{E}_{\text{total}\varphi}(r,\varphi,h) &= \Delta V_{\text{CMSS}} \boldsymbol{T}_{\Delta\text{VCMSS}\varphi}(r,\varphi,h) \\ &\quad + \Delta V_{\text{CMSO}} \boldsymbol{T}_{\Delta\text{VCMSO}\varphi}(r,\varphi,h)\end{aligned} \tag{18}$$

where $\boldsymbol{E}_{\text{total}\varphi}$ represents the total horizontal field intensity generated by $\Delta V_{\text{CMSS}}$ and $\Delta V_{\text{CMSO}}$.

The driving voltage values can be obtained through the above measurement, but it is difficult to evaluate the radiation transfer functions through the analytical antenna calculation. Therefore, this article uses the electromagnetic simulation tool for its reasonable calculations. For this purpose, the specific modeling and simulation process are introduced in Section IV.

## IV. Electromagnetic Modeling and Transfer Function Simulation of the Radiator With Two Driving Sources

The 3-D modeling of the radiator composed of shielded cables and PCB is first presented using the Feko electromagnetic software, and then the simulation results of the spatial radiation transfer functions are introduced in this section.

### A. Three-Dimensional Electromagnetic Model of the Radiator With Two CM Driving Sources

The horizontal shielded cables and PCBs form an unintentional radiator with a complex structure. Establishing an accurate 3-D electromagnetic simulation model is necessary to precisely

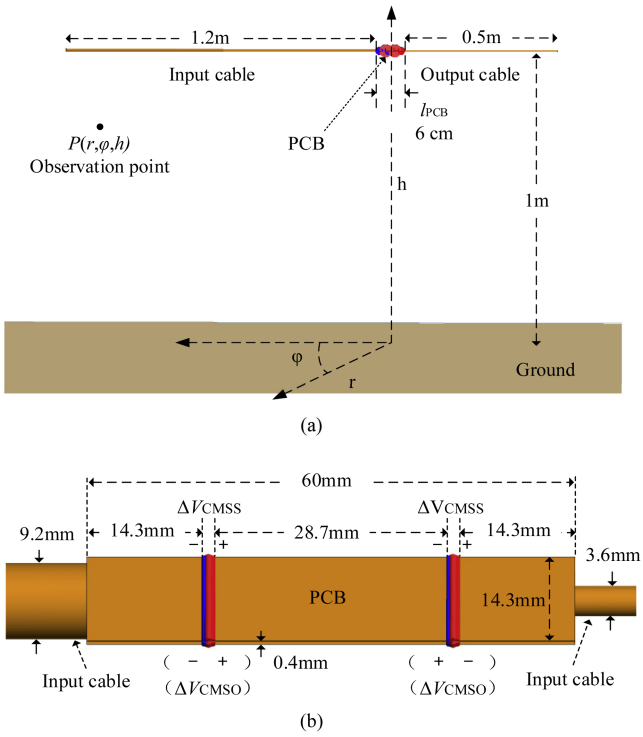


Fig. 7. Three-dimensional electromagnetic simulation model utilized for the shielded cables and PCBs. (a) Overall view of the Feko model. (b) Enlarged PCBs model of the converter.

determine the radiation transfer functions of the parasitic radiator. Feko software is a powerful full-wave 3-D electromagnetic simulation tool that supports various algorithms such as the method of moments and finite element analysis, and is particularly suitable for modeling and analyzing various antennas. This study uses it for modeling and simulating transfer functions [19].

As a practical example, the main dimensions of the cables and PCBs in Fig. 6 are as follows. The input cable of the converter, including the battery's shielded shell, is 1.2 m long, and its external diameter is 9.2 mm. The output cable, including the load's shielded shell, is 0.5 m long, and its external diameter is 3.6 mm. The entire PCB of the low-side converter is about 6.0 cm long, 1.43 cm wide, and 0.4 mm thick. The PCB is roughly divided into three segments with lengths of 14.3, 28.7, and 14.3 mm. During the electromagnetic modeling of the unintentional radiator, the input cable, output cable, and PCBs are modeled according to the above dimensions, and the insulation layers of the cables are ignored. Fig. 7(a) illustrates the entire 3-D electromagnetic model of the radiator using Feko Suite 7.0 software. In this figure, the height $h$ is set as 1 m, and the main dimensions of the cables and PCBs are also specified clearly. The red-blue dots in the middle of the figure represent the CM driving voltages along the main circuit PCBs. The bottom plane is the metal ground, and the cylindrical coordinates are also demonstrated. Fig. 7(b) illustrates the magnified electromagnetic model of the PCBs of the low-side Buck converter. The detailed dimensions of PCBs are also provided, and the two types of CM subdriving sources are clearly marked as red-blue stripes, which represent just red-blue dotted marks in Fig. 7(a).

### B. Radiation Transfer Function Simulations at Different Observation Positions

According to the structure of Fig. 7(b), the voltage of the two driving sources $\Delta V_{\mathrm{CMSS}}$ should be set as $+1$ and $+1$ V in the 3-D Feko model, then the horizontal field intensity at a certain observation point in space can be simulated and calculated. In fact, the value of this field intensity is just the horizontal radiation transfer function $\boldsymbol{T}_{\Delta\mathrm{VCMSS}\varphi}$ of the driving source $\Delta V_{\mathrm{CMSS}}$. In the present study, three observation points are selected as typical observation positions: ($r$ = 10 m, $\varphi$ = 90°, $h$ = 1 m), (10 m, 90°, 4 m), and (10 m, 45°, 1 m). The magnitude and phase curves of the horizontal transfer function $\boldsymbol{T}_{\Delta\mathrm{VCMSS}\varphi}$ are obtained via Feko electromagnetic simulation at the observation point (10 m, 90°, 1 m), and they are demonstrated in blue in Fig. 8(a) and (b), respectively.

Similarly, the horizontal transfer function $\boldsymbol{T}_{\Delta\mathrm{VCMSO}\varphi}$ under the driving sources $\Delta V_{\mathrm{CMSO}}$ can be simulated after setting the two $\Delta V_{\mathrm{CMSO}}$ voltage sources as $+1$ and $+1$ V in Fig. 7(b). The simulated magnitude and phase curves are also demonstrated in red in Fig. 8(a) and (b), respectively. It can be seen that the magnitude of the $\boldsymbol{T}_{\Delta\mathrm{VCMSO}\varphi}$ is generally smaller than that of the $\boldsymbol{T}_{\Delta\mathrm{VCMSS}\varphi}$, indicating that its radiation capacity is smaller than that of the former. This actually corresponds to the direction of the CM currents on the input and output cables.

Furthermore, Figs. 9 and 10 demonstrate the Feko simulated horizontal transfer function curves produced by $\Delta\mathrm{V}_{\mathrm{CMSS}}$ and $\Delta\mathrm{V}_{\mathrm{CMSO}}$ at (10 m, 90°, 4 m) and (10 m, 45°, 1 m), respectively. Although their magnitudes are dissimilar, the magnitude curves of $\boldsymbol{T}_{\Delta\mathrm{VCMSO}\varphi}$ are overall smaller than that of $\boldsymbol{T}_{\Delta\mathrm{VCMSS}\varphi}$.

To verify the effectiveness of Feko simulation, this study utilizes ANSYS HFSS electromagnetic software to simulate the magnitude transfer functions at every observation point too [20]. The results of the HFSS-based simulations are also exhibited with dashed green and light purple curves in Figs. 8(a)–10(a), and it can be seen that the Feko results are reasonably consistent with the HFSS results in general.

## V. Experiment and Verification

To validate the proposed far-field radiation models and prediction method, a prototype of a 30-MHz low-power VHF low-side Buck converter is fabricated and described in this section. The main specifications and structure of the prototype are first introduced, and then the radiation prediction and verification are carried out. The radiation characteristics of different exciting sources are investigated, and two effective suppression designs are implemented at the end.

### A. 30-MHz Low-Side Buck Converter Prototype

Fig. 11 illustrates the prototype of the 30 MHz low-side Buck converter fabricated in this study. This power converter uses GaN chips to achieve high-speed switching of several tens of MHz. The key components and PCB traces are generally the same, as demonstrated in Fig. 4(b), and the main geometric dimensions are also mentioned in the photograph. It should be noted that the PCB length between GaN and $L$ is relatively long, which

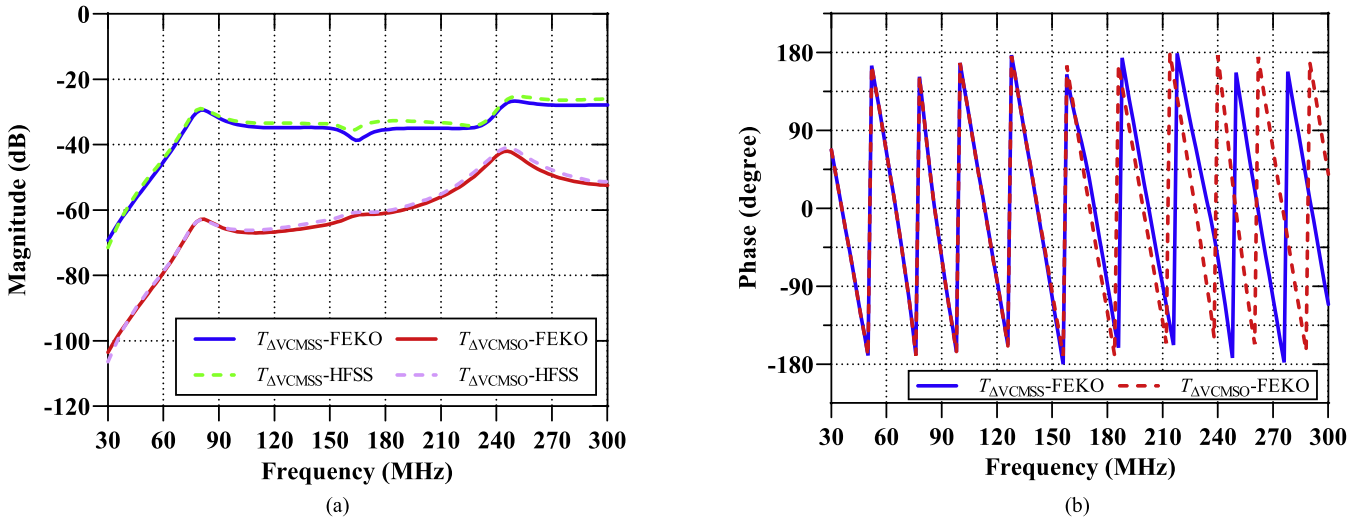


(a) (b)

Fig. 8 Simulated horizontal radiation transfer function curves $T_{\varphi}$ at the observation point (10 m, 90°, 1 m). (a) Magnitude curves. (b) Phase curves.

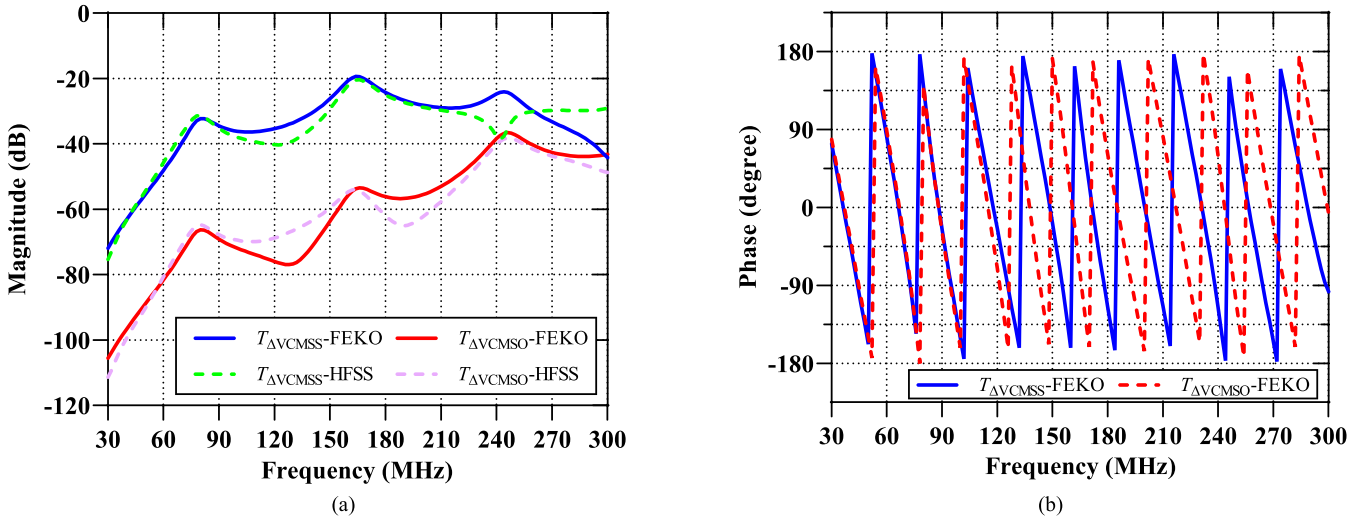


(a) (b)

Fig. 9 Simulated horizontal radiation transfer function curves $T_{\varphi}$ at the observation point (10 m, 45°, 1 m). (a) Magnitude curves. (b) Phase curves.

is supposed to be closer to the QTEM mode and also leads to increased switching oscillation. The low-side GaN is placed on the top layer of the PCB for ease of installation and welding, but it is modest and has little impact on the CM driving source and radiation. Therefore, it is still evaluated here using the layout of Fig. 4(b).

The main performance indicators and parameters of the low-side Buck converter are listed in Table I. In this table, $C_1$ denotes paralleled ceramic capacitors with $C_{\rm in}$ to improve high-frequency impedance. $C_2$ acts similarly and is connected in parallel to $C_{\rm out}$. The PCB of the converter represents a two-layer thin plate with a thickness of only 0.4 mm, which reduces the radiation of the DM current of the main circuit as small as possible.

Fig. 12 depicts the actual layout and main geometrical parameters of the low-side Buck converter with shielded cables, which are actually identical to those presented in Fig. 7. The input and output cables of the converter adopt coaxial cable to effectively eliminate the influence of DM radiation. The input cable model

TABLE I
MAIN PERFORMANCE INDICATORS AND PARAMETERS

| Parameter (symbol) | Magnitude (unit) |
|---|---|
| DC input voltage ($V_{\rm in}$) | 12 (V) |
| DC output voltage ($V_{\rm out}$) | 6.5 (V) |
| Output load | 10 (Ω) |
| Switching frequency ($f_s$) | 30 (MHz) |
| Inductor ($L$) | 0.56 (μH) |
| Capacitor ($C_{\rm in1}$ $C_{\rm out1}$) | 47 (μF) |
| Capacitor ($C_1 - C_2$) | 0.022 (μF) |
| Duty cycle ratio | 50 % |
| GaN (M) | GS61004B, 100 V, 38 A |
| Diode ($D$) | PMEG4020EPK×2, 40 V, 2 A |

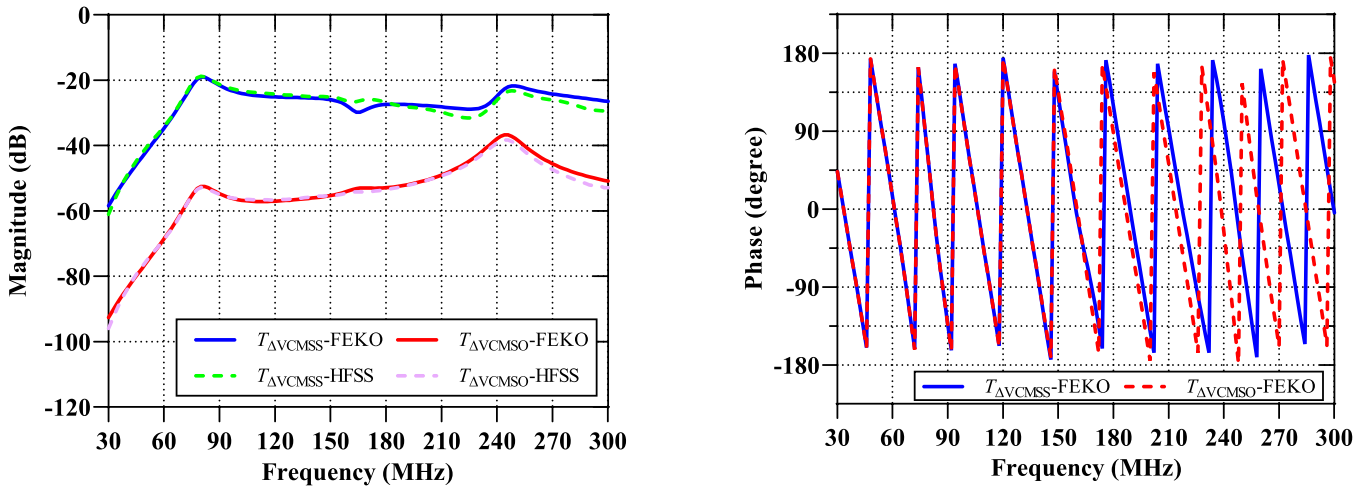


(a) (b)

Fig. 10. Simulated horizontal radiation transfer function curves $T_{\varphi}$ at the observation point (10 m, 90°, 4 m). (a) Magnitude curves. (b) Phase curves.

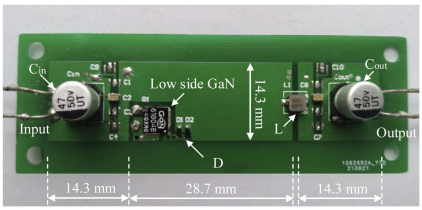


Fig. 11. 30-MHz VHF low-side Buck converter prototype.


Fig. 12. Actual layout of the low-side Buck converter and its shielded cables.

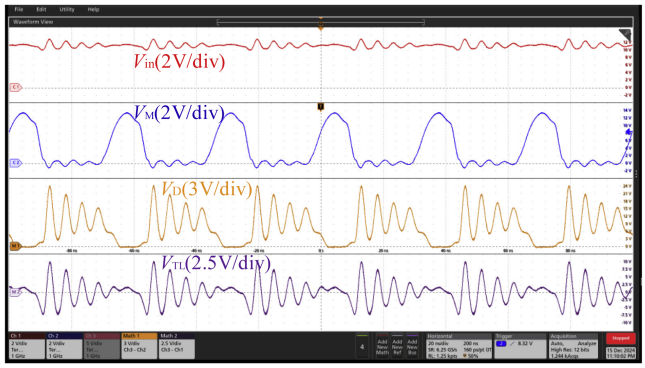


Fig. 13. Measured voltage waveform plots of $V_{\rm in}$, $V_M$, $V_D$, and $V_{\rm TL}$.

is taken as RG-214/U, whose outer shielding diameter is 9.2 mm, and the output cable model is taken as RG-58/U, whose outer shielding diameter is 3.6 mm. In this study, the method of connecting 8 small AAA 1.5 V cylindrical lithium batteries in series and applying copper foil shielding with a diameter almost the same as the input coaxial line at the same time is effectively employed to avoid the nonideal effect caused by a common large-volume 12 V power supply battery; similarly, the above-mentioned copper foil shielding method is utilized for the load resistance of 10 Ω to also avoid the influence of DM radiation. Finally, the input cable with the battery is 1.2 m long, the output cable with the load is 0.5 m long, and the main circuit PCB is 6 cm long. A 6-V button lithium battery powers the driving signal circuit, which is housed in a thin copper shell. The copper shell is located just below the PCB and is connected to the negative electrode of $V_{\rm in}$, and the driving signal is transmitted to the GaN gate via short wires.

### B. CM Far-Field Radiation Prediction and Verification

*1) CM Driving Sources and Their Spectrum:* The main CM driving voltages of the low-side Buck converter ($\Delta V_{\rm CML}$ and $\Delta V_{\rm CMR}$) can be directly measured by a digital oscilloscope, that is, $V_{\rm os'}$ and $V_{\rm os}$ in Fig. 6. The same-direction driving source $\Delta V_{\rm CMSS}$, and the opposite-direction driving source $\Delta V_{\rm CMSO}$ can be calculated by (5) and (6), respectively. Then, the fast Fourier transform (FFT) technique is utilized to obtain their alternating spectrum.

Fig. 13 demonstrates the measured voltage waveforms of $V_{\rm in}$, $V_M$, $V_D$, and $V_{\rm TL}$ by a Tek MSO 44 oscilloscope with an input impedance of 10 M//3.9 pF. The oscillation of the diode voltage $V_D$ in the figure is somewhat large, which is essentially attributed to the fact that the PCB trace length is not deliberately minimized. Overall, the waveforms show that the VHF converter is working properly. Fig. 14 illustrates more of the measured CM voltage waveforms of $\Delta V_{\rm CML}$ and $\Delta V_{\rm CMR}$ by the Tek MSO 44.

Fig. 15 demonstrates the calculated CM voltage waveforms of $\Delta V_{\rm CMSS}$ and $\Delta V_{\rm CMSO}$. The spectrum of $\Delta V_{\rm CMSS}$ and $\Delta V_{\rm CMSO}$ can be evaluated via the FFT-based approach, and

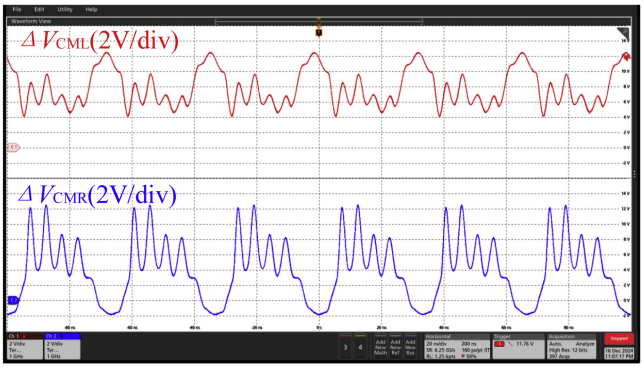


Fig. 14. Measured voltage waveform plots of $\Delta V_{\mathrm{CML}}$ and $\Delta V_{\mathrm{CMR}}$.

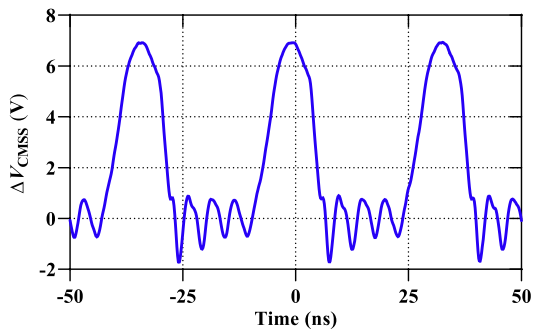


(a)

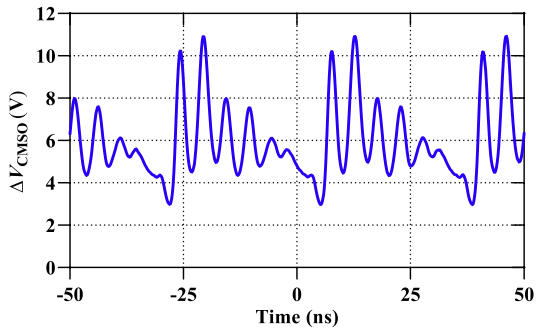


(b)

Fig. 15. Calculated voltage waveforms of $\Delta V_{\mathrm{CMSS}}$ and $\Delta V_{\mathrm{CMSO}}$. (a) Calculated $\Delta V_{\mathrm{CMSS}}$. (b) Calculated $\Delta V_{\mathrm{CMSO}}$.

their magnitude and phase curves are illustrated in Figs. 16 and 17, respectively.

It should be noted that the voltage divider resistor $R$ of diode $D$ in parallel is set to 100 Ω, so the load effect impact of the oscilloscope probes can be rationally ignored in the present investigation. This also means that the calculated spectra in Figs. 16 and 17 are almost the same as their actual values when the oscilloscope probes are disconnected.

### *2). CM Radiation Prediction and Verification*

Taking into account the spectra of CM driving voltages and the horizontal transfer functions $\boldsymbol{T}_{\varphi}$ in (18), the horizontal field intensity formed by the same-direction driving source $\Delta V_{\mathrm{CMSS}}$,

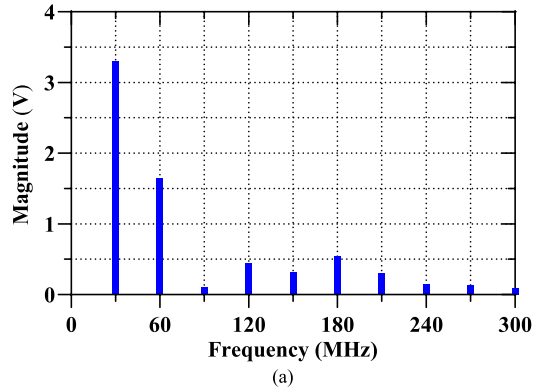


(a)

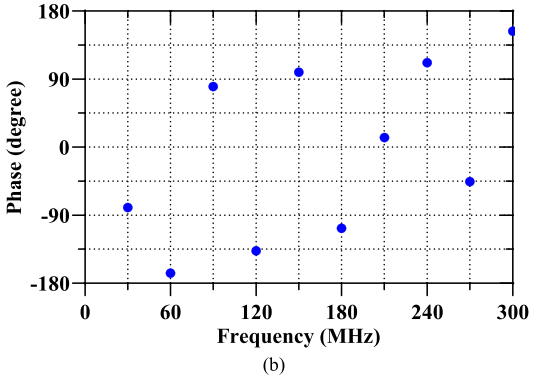


(b)

Fig. 16. Calculated alternating spectrum of magnitude and phase of $\Delta V_{\mathrm{CMSS}}$ (a) Magnitude plot. (b) Phase plot.

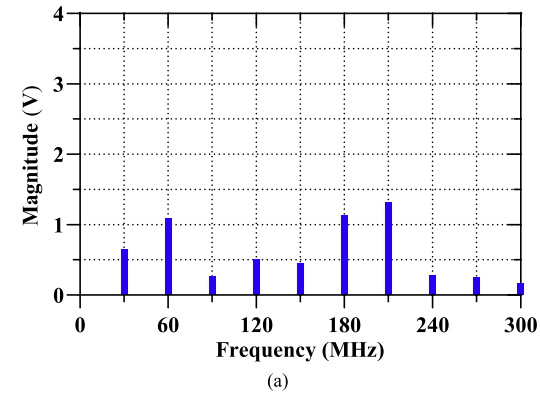


(a)

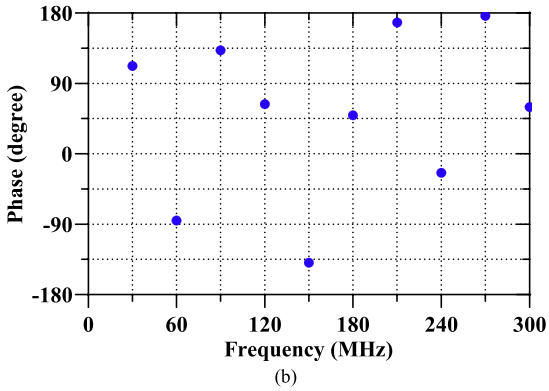


(b)

Fig. 17. Calculated alternating spectrum of magnitude and phase of $\Delta V_{\mathrm{CMSO}}$ (a) Magnitude plot. (b) Phase plot.

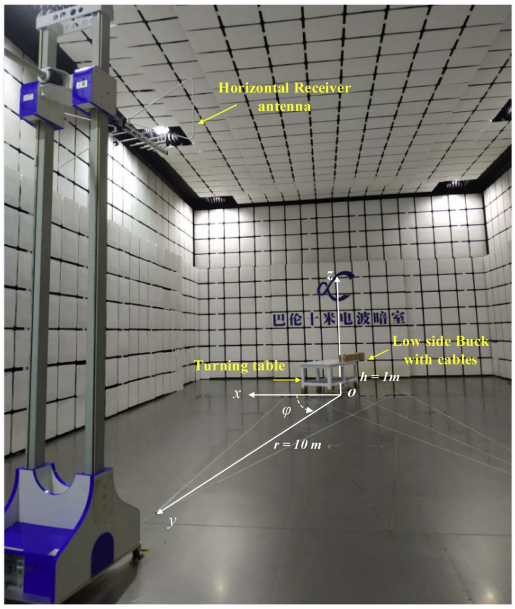


Fig. 18. Radiation test photograph of the low-side Buck with horizontal cables in a 10 m semi-anechoic chamber.

the field intensity formed by the opposite-direction driving source $\Delta V_{\mathrm{CMSO}}$, and the total horizontal field intensity $E_{\mathrm{total}\varphi}$ can be predicted.

The total horizontal field intensity $E_{\mathrm{total}\varphi}$ can also be measured at a standard RE test site. The actual scenario of a far-field RE test in a 10 m commercial semi-anechoic chamber has been presented in Fig. 18. The coordinate system in Fig. 18 is the same as that in Fig. 7(a).

Fig. 19 illustrates the measured and predicted horizontal electric field intensity at three typical observation positions. The cylindrical coordinates of the observation positions are represented by (10 m, 90°, 1 m), (10 m, 45°, 1 m), and (10 m, 90°, 4 m). It can be seen that the predicted electric intensities are generally consistent with the measured electric intensities. At most harmonic frequencies, the prediction error is approximately 3–6 dB, with a few exceptions at frequency points below 300 MHz.

To quantify and evaluate the consistency between the predicted data and the measured data, the feature selective validation methodology is most commonly used [21]. The overall consistency results are very good, indicating that the predicted data exhibit very good consistency. Therefore, the above-mentioned measurement results generally confirm the feasibility and validity of the proposed prediction method.

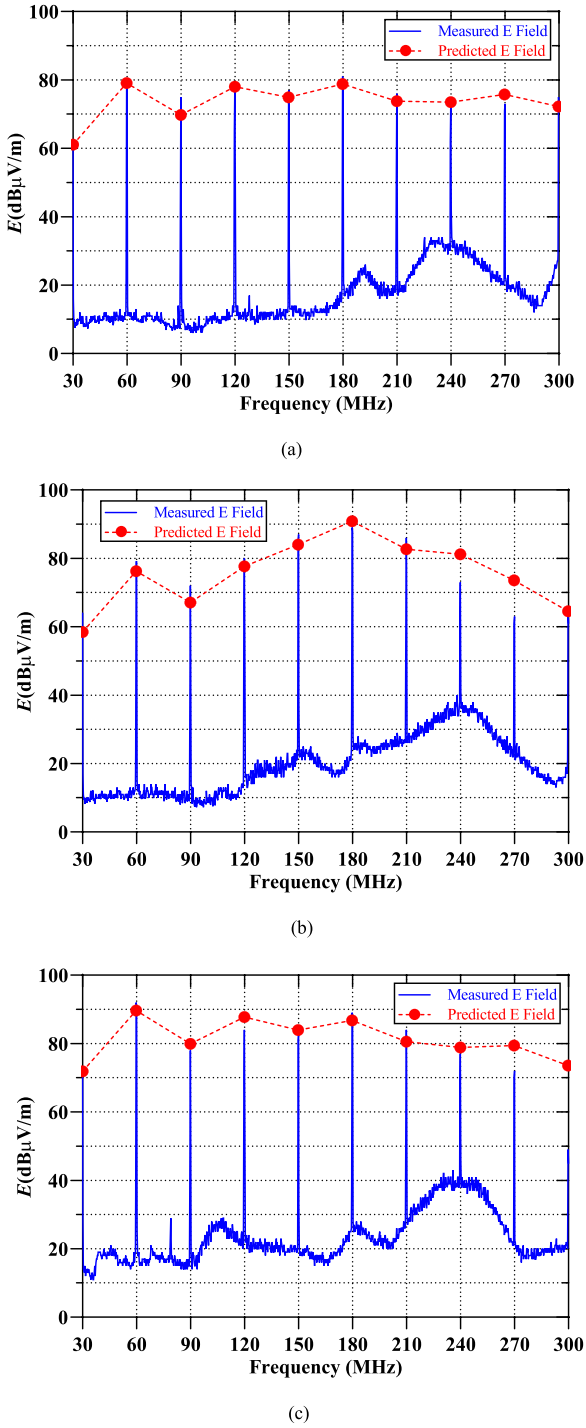


Fig. 19. Predicted and measured electric intensities in a 10 m semi-anechoic chamber. (a) $r = 10$ m, $\varphi = 90°$, $h = 1$ m. (b) $r = 10$ m, $\varphi = 45°$, $h = 1$ m. (c) $r = 10$ m, $\varphi = 90°$, $h = 4$ m.

### C. Radiation Roles Analysis of Two Type CM Driving Sources

Based on the above-mentioned prediction model, the role of the specific radiation $\Delta V_{\mathrm{CMSS}}$ and $\Delta V_{\mathrm{CMSO}}$ can be analyzed separately. Fig. 20 illustrates the predicted radiation field intensity generated by $\Delta V_{\mathrm{CMSS}}$ and $\Delta V_{\mathrm{CMSO}}$ in the typical position (10 m, 90°, 1 m). The plotted results are indicative of the fact that the radiation field generated by $\Delta V_{\mathrm{CMSS}}$ is generally much higher than that of $\Delta V_{\mathrm{CMSO}}$ in most of the frequency bands from 30 to 300 MHz. The reason behind this fact is that the parasitic antenna between the input cable and the output cable exhibits a higher radiation efficiency than the parasitic antenna between the PCBs and the input/output cables. Although $E_{\Delta \mathrm{VCMSO}\varphi}$ reaches its maximum at the points of 210 and 240 MHz, the magnitude of $E_{\mathrm{total}\varphi}$ is still close to $E_{\Delta \mathrm{VCMSS}\varphi}$.

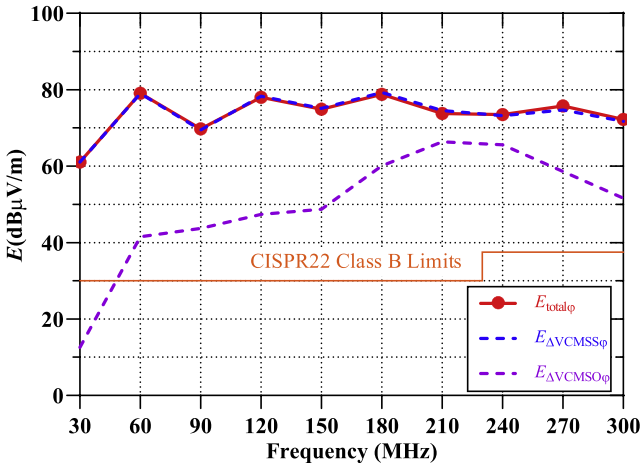


Fig. 20. Predicted electric field intensity and its components at the position of (10 m, 90°, 1 m).

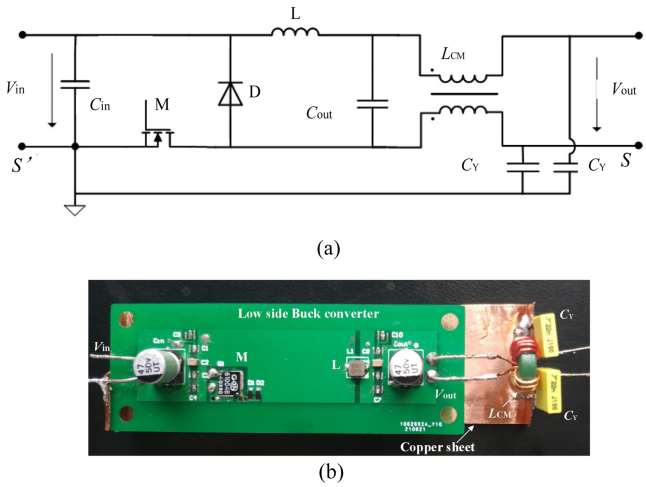


Fig. 21. CM filter suppression design at the output port. (a) Circuit principle of CM EMI filter. (b) Actual top-view of $L_{\mathrm{CM}}+C_Y$ CM filter.

It should be noted here that the radiation structure demonstrated in Fig. 6 can also be considered as an asymmetric antenna and its excitation source is the voltage $V_M$ passing through the GaN switch from the traditional point of view [16]. The voltage waveform of $2\Delta V_{\mathrm{CMSS}}$, i.e., $V_{\mathrm{ss'}}$ can be found to be very close to the voltage waveform of $V_M$ according to the circuit diagram of Fig. 4(b) and the measured voltage waveforms in Figs. 13 and 15(a), so the proposed radiation model could include and explain the traditional radiation analysis model. In addition, this new proposed model is able to clearly identify the second cause of far-field radiation exceeding the CISPR22 Class B standard from 75 to 300 MHz, which is the radiation $E_{VCMSO\varphi}$ generated between the high d$v$/d$t$ conductors in the main circuit and the input/output cables. From the perspective of radiation suppression design for the EMC certification of the product, all causes must be considered and carefully investigated. Therefore, this new model provides a more accurate physical picture and could promote an up-to-date understanding of EMI for power designers [22].

### D. CM Far-Field Radiation Suppression Designs

For the CM driving source $\Delta V_{\mathrm{CMSS}}$, the low-side Buck converter is directly applied between the input cable shield layer and the output cable shield layer, so that strong radiation is easily generated. This voltage is physically generated by the $V_M$ of GaN and cannot be reduced simply. For instance, an RC snubber design could lessen part of the spectrum of $V_M$, thus reducing the far-field radiation, but it increases the Buck converter loss during switching. To reduce the parasitic radiator driving voltage, this study proposes two suppressions. The first is to place a CM filter between the input and output cables, and the second is to change the position of the inductor $L$ to the negative bus.

*1). CM Filter Suppression Design:* Fig. 21(a) demonstrates the principle of the CM filter and its position, which consists of a high-frequency CM choke $L_{\mathrm{CM}}$ and two $C_Y$ capacitors. Its suppression principle is briefly explained as follows: The CM driving voltage $2\Delta V_{\mathrm{CMSS}}$ is mainly borne by $L_{\mathrm{CM}}$, while $2C_Y$ further causes a voltage decrease of $V_{ss'}$. The snapshot of the low-side Buck converter with the filter is presented in Fig. 21(b). Here, a large metal ground board is utilized to reduce the ground impedance of the $C_Y$ capacitors.

The inductance of this CM choke is 0.59 mH, it has a Mn–Zn toroidal core and a 10-turn coil, and the $C_Y$ is set as 22 nF. Fig. 22 demonstrates the CM filter's suppression effect on the CM voltage $V_{\mathrm{SS'}}$ and the radiation at the typical position (10 m, 90°, 1 m). According to the measured voltage waveforms in Fig. 22(a), it can be seen that the amplitude of $V_{\mathrm{SS'}}$ significantly decreases after applying the CM filter. From the measured radiation intensity in Fig. 22(b), it can also be seen that the radiation intensity is reduced by more than 20 dB between 30 and 210 MHz and is also reduced up to 300 MHz. The test results reveal that this CM filter design provides a good suppression effect.

*2). Position Change Design of the Inductor* L*:* Fig. 23(a) shows the suppression design of changing the position of the inductor $L$ to its negative bus. Fig. 23(b) and (c) illustrates the actual prototype of this suppression design. In this suppression design, the PCB size is basically taken the same as Fig. 9, the positive bus trace is considered on the top layer, and the switch $M$ and the inductor $L$ are welded at the bottom layer.

Since the voltage $V_M$ in the switch $M$ is directly borne by the inductor $L$, the $V_{\mathrm{ss'}}$ voltage is substantially reduced, which could effectively lessen the CM radiation. In other words, $V_{\mathrm{ss'}}$ would be equal to $V_{\mathrm{out}}$ -$V_{\mathrm{in}}+V_{\mathrm{TPCB}}$ as shown in Fig. 23(a), and $V_{\mathrm{in}}$ and $V_{\mathrm{out}}$ are close to dc, so, $V_{\mathrm{ss'}}$ is chiefly determined by $V_{\mathrm{TPCB}}$. The positive bus impedance is relatively small, resulting in a small voltage drop value related to $V_{\mathrm{TPCB}}$. Fig. 24 demonstrates the suppression effect of the new position design on $V_{\mathrm{SS'}}$ and the radiation at the typical position of (10 m, 90°, 1 m). According to the measured voltage waveforms in Fig. 24(a), it can be seen that the amplitude of $V_{\mathrm{SS'}}$ clearly decreases when $L$ is moved to the negative bus side. From the measured radiation intensity in Fig. 24(b), it can also be seen that the radiation intensity is reduced by more than 10 dB between 30 and 180 MHz, except for a 5 dB reduction at 90 MHz. The results of this experiment

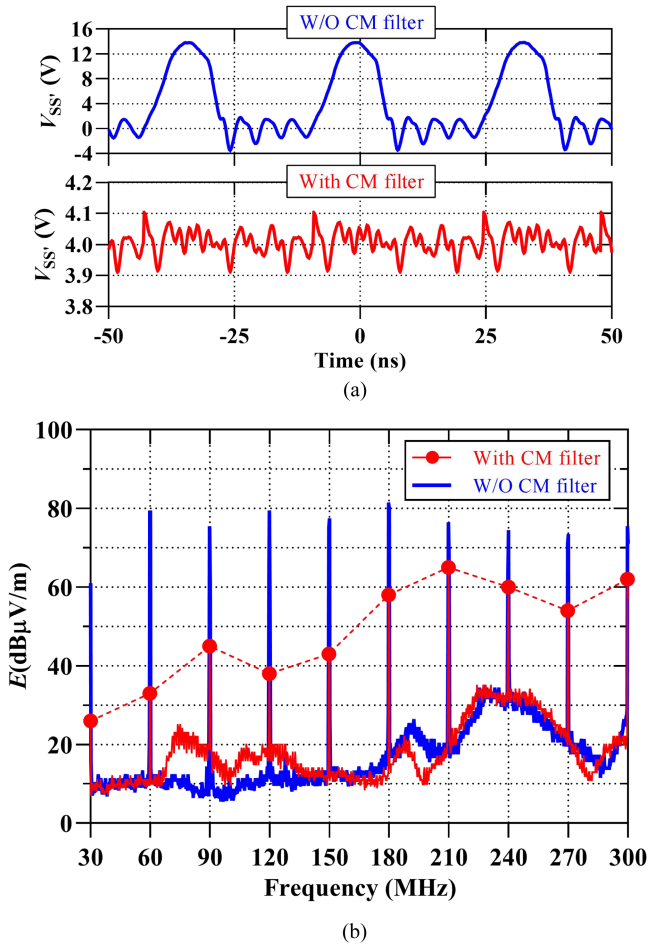


Fig. 22. Measured $V_{SS'}$ and far-field electric field intensity at the position of (10 m, 90°, 1 m) before, and after inserting the CM filter. (a) $V_{SS'}$ voltage waveforms. (b) Measured far-field electric field intensity.

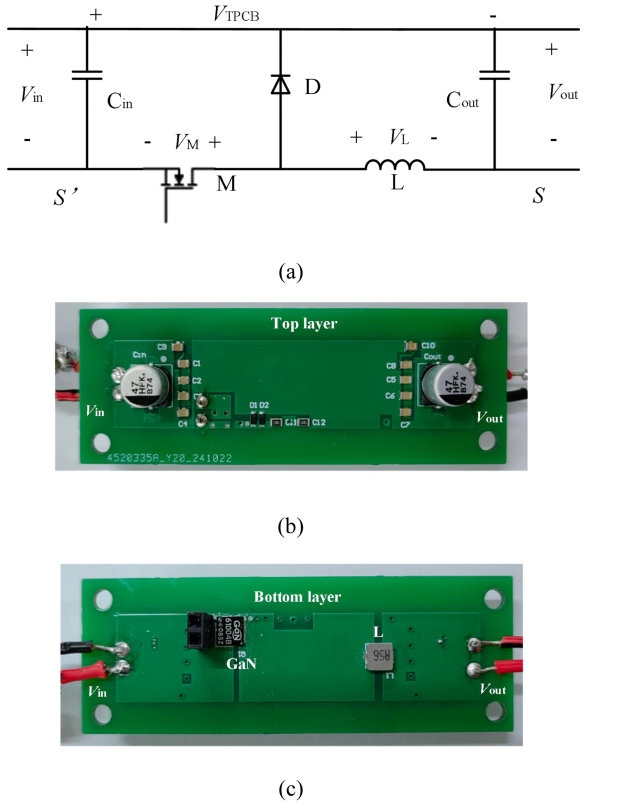


Fig. 23. L position change design. (a) Circuit principle. (b) Top layer photograph of the improved Buck converter. (c) Bottom layer photograph of the improved Buck converter.

show that the inductor's position change design also provides a good suppression effect.

## VI. Discussion

The radiation measurement results of the low-side Buck converter in Section V show that the proposed prediction methodology is effective. However, the predictions are made under certain conditions such as fixed power cable and layout, PCB layout, and load. For a real product, there may be large changes in the physical structure of the main circuit, component size, cable length, and diameter. These changes will undoubtedly cause variations in the voltage of the switches, input or output voltage ripple, as well as the distribution and intensity of far-field radiation. The detailed analysis, testing, and study of the specific influence of these factors on far-field radiation definitely brings more technical challenges and requires more in-depth work. This is also beyond the scope and purpose of this article at present. Therefore, as an effort, this section essentially analyzes and discusses the influence of cable and PCB size factors on the radiation transfer functions from 30 to 150 MHz.

### A. Influence of the Output Cable Length for the Case of Unchanged Input Cable and PCB Dimensions

*1). Transfer Function $T_{\Delta VCMSS\varphi}$ Simulations and Discussions:* By keeping the input cable length of 1.2 m and the PCB length of 6 cm, Feko software is then utilized to simulate the transfer functions $\boldsymbol{T}_{\Delta \mathrm{VCMSS}\varphi}$ for various scenarios where the output cable length is set equal to 0.1, 0.5, and 1.2 m. Fig. 25 illustrates the simulated magnitude-frequency curves of the transfer function $\boldsymbol{T}_{\Delta \mathrm{VCMSS}\varphi}$ at a typical observation point with coordinates (10 m, 90°, 1 m). The plotted results indicate that as the output cable length increases, the frequency of the first peak decreases, and at the same time, the magnitude of the transfer function before the first peak increases. This also means that shortening the cable length is beneficial to reduce the radiation efficiency of the SMPS in the lower frequency band.

*2). Transfer Function $T_{\Delta VCMSO}$ Simulations and Discussions:* By keeping the input cable length of 1.2 m and the PCB length of 6 cm, the transfer functions $T_{\Delta \mathrm{VCMSO}\varphi}$ are simulated similarly in the presence of the output cable lengths of 0.1, 0.5, and 1.2 m. Fig. 26 demonstrates the simulated magnitude-frequency curves of the transfer function at the observation point with coordinates (10 m, 90°, 1 m). The illustrated results reveal that as the length difference between the input and output cables decreases, the value of the radiation transfer function generally lessens. In addition, as the output cable length reaches the same

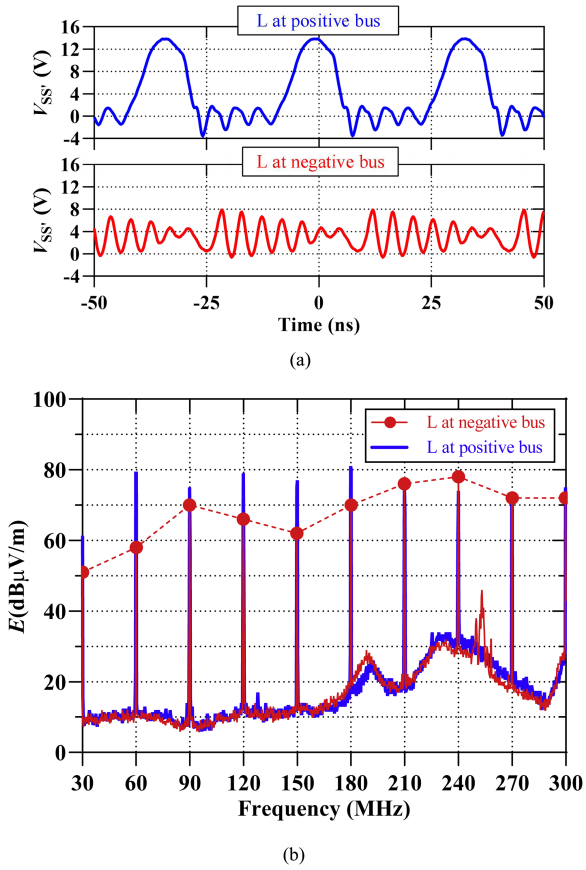


Fig. 24. Measured $V_{SS'}$ and far-field electric field intensity before and after applying the new topology. (a) $V_{SS'}$ voltage waveforms. (b) Measured far-field electric field intensity.

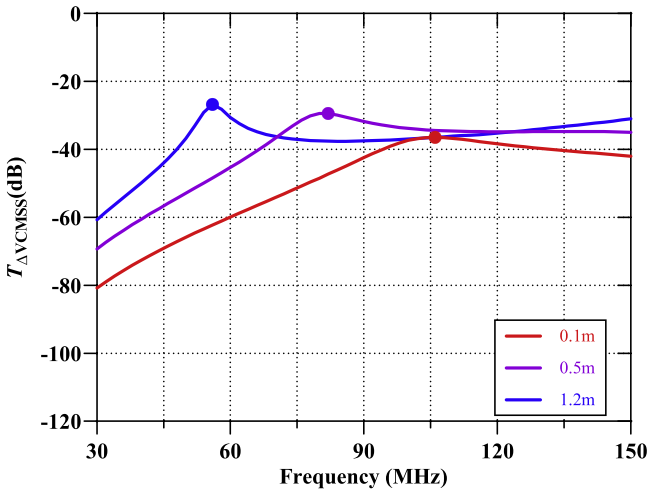


Fig. 25. Simulated transfer functions $T_{\Delta\mathrm{VCMSS}\varphi}$ in the presence of various lengths of the output cable.

1.2 m as the input cable, the radiation transfer function drastically reduces below 100 MHz. This indicates that designing equal-length input and output cables is substantially beneficial to reduce $T_{\Delta\mathrm{VCMSO}\varphi}$. It is also worth mentioning that this feature is significantly different from $T_{\Delta\mathrm{VCMSS}\varphi}$.

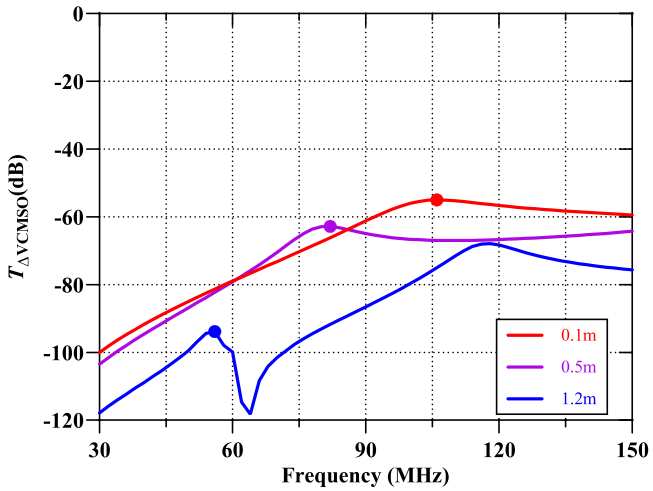


Fig. 26. Simulated transfer functions $T_{\Delta\mathrm{VCMSO}\varphi}$ in the presence of various lengths of the output cable.

### *B. Influence of the PCB Dimensions for the Case of Unchanged Input Cable and Output Cable Size*

*1). Transfer Function $T_{\Delta VCMSS\varphi}$ Simulations and Discussions:* By taking the input and output cable lengths of 1.2 and 0.5 m, respectively, the transfer functions $T_{\Delta\mathrm{VCMSS}\varphi}$ can also be simulated for various scenarios where the lengths of the main circuit of PCB are set equal to 1.4, 6, and 10 cm. Fig. 27(a) illustrates the simulated magnitude-frequency curves of the transfer function $T_{\Delta\mathrm{VCMSS}\varphi}$ at the observation point of coordinates (10 m, 90°, 1 m). It is observed that both the first peak frequency and the radiation efficiency remain essentially unchanged when the PCB size is much smaller than the input and output cables, that is, the resulting impact is not significant when the PCB size is relatively small. So, the PCB dimension is further altered to examine its radiation effect.

The PCB dimensions are set to 6 cm in length with 1.4, 6, and 10 cm in width, respectively, and the simulation results are shown in Fig. 27(b). It is observed that the effect is also not significant when the PCB size is relatively small.

*2). Transfer Function $T_{\Delta VCMSO\varphi}$ Simulations and Discussions:* Through maintaining the input cable length of 1.2 m and the output cable length of 0.5 m, the transfer functions $\mathrm{T}_{\Delta\mathrm{VCMSO}\varphi}$ are also simulated for the different scenarios, mainly considering the PCB length of the main circuit equal to 1.4, 6, and 10 cm. Fig. 28(a) illustrates the simulated magnitude-frequency curves of the transfer function $\mathrm{T}_{\Delta\mathrm{VCMSO}\varphi}$ at an observation point of coordinates (10 m, 90°, 1 m). The plotted results are indicative of the fact that the frequency of the first peak slightly decreases when the length of the PCB length increases. However, the magnitude of the curves substantially reduces, which is very different from the case of $\mathrm{T}_{\Delta\mathrm{VCMSS}\varphi}$ in the previous section. This simulation reveals that the size of the high dv/dt conductor area has a noticeable impact on the $\mathrm{T}_{\Delta\mathrm{VCMSO}\varphi}$ mode.

In continuing, the PCB dimension is further altered to examine its radiation influence. To this end, let us set the PCB length as

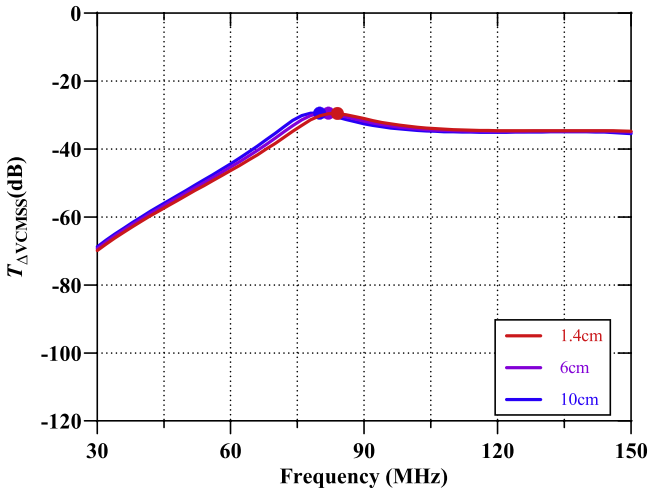


(a)

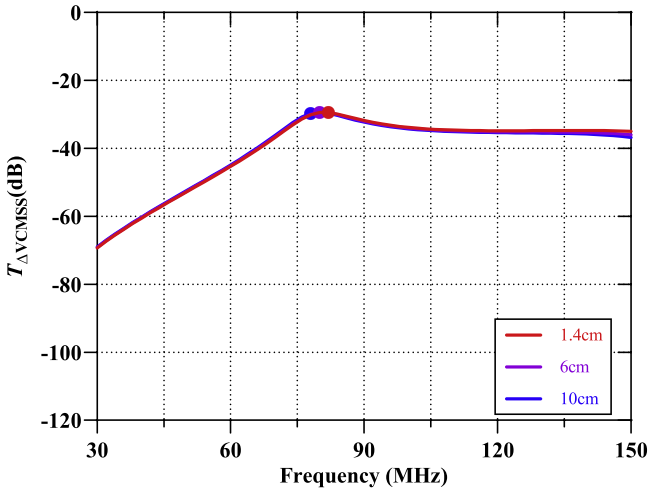


(b)

Fig. 27. Simulated transfer functions $T_{\Delta \mathrm{VCMSS}\varphi}$ in the presence of various PCB dimensions. (a) Effect of the PCB length. (b) Effect of the PCB width.

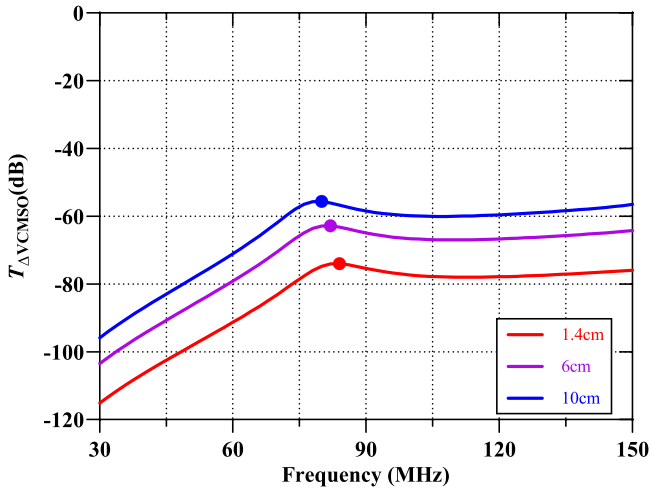


(a)

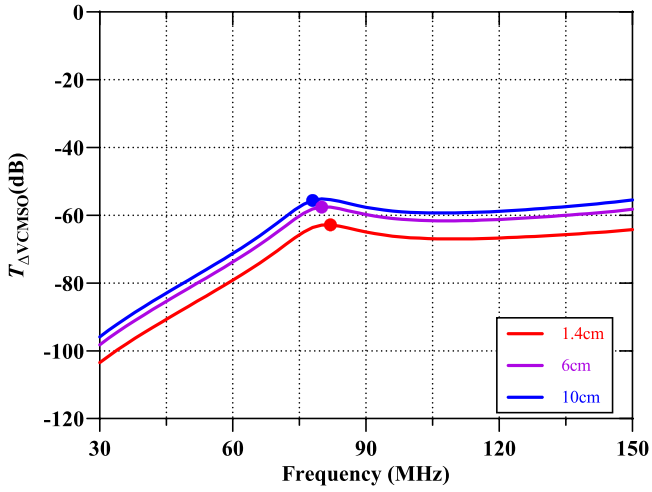


(b)

Fig. 28. Simulated transfer functions $T_{\Delta \mathrm{VCMSO}\varphi}$ in the presence of various PCB dimensions. (a) Various PCB lengths. (b) Various PCB widths.

6 cm with 1.4, 6, and 10 cm width, and the simulation results are presented in Fig. 28(b). The results reveal that the transfer function $T_{\Delta \mathrm{VCMSO}\varphi}$ exhibits a similar trend as the previous Fig. 28(a).

According to the previous simulation results, it can be seen that the changes in cable and PCB dimensions have dissimilar effects on the radiation transfer functions in the presence of various driving modes, and therefore, their impact on the overall radiation intensity is definitely dissimilar. In general, the input and output cables have a greater impact on CM radiation, which also indicates that more attention should be paid to the control of their driving sources during design stage. Although the number of simulations mentioned is limited, the Feko simulation results not only show the complexity of the radiation mechanisms and phenomena but also demonstrate the role and useful value of electromagnetic simulation in the quantitative study of power electronics radiation, which is very worthy of further investigation and application.

## VII. Conclusion

This study investigates the CM driving sources of a low-side Buck converter in-depth, utilizes electromagnetic simulation tools to obtain the radiation transfer functions of the unintentional radiators, and finally achieves an effective prediction of the converter' s CM far-field radiation. The main conclusions and scientific contributions are summarized as follows.

1) The CM voltage driving sources of the low-side Buck converter are methodically examined and quantified. The far-field radiation formulas of horizontal cables with dual driving sources are suitably derived after rationally decomposing these CM driving sources into same and opposite direction modes.
2) The CM far-field radiation prediction of a 30-MHz low-side Buck converter with horizontal shielded cables is performed via an appropriately proposed prediction approach, and the efficacy of the prediction performance is verified in the case of 10 m length via experimental findings in the interval of 30–300 MHz.

3) The performed investigation and analysis demonstrate that the main CM driving source of the low-side Buck converter possesses the same-direction driving source, and the opposite-direction source are also able to cause excessive radiation emission.
4) The CM filter design and inductor position change design are methodically proposed, and the effectiveness of the new suppression designs are verified using 10-m experimental measurements.
5) The Feko electromagnetic tool is utilized to quantitatively simulate the various effects of changing the cable and PCB size on the radiation transfer functions of the two driving modes. In general, the smaller size helps to reduce the magnitude of the transfer function in the lower-frequency range.

This research proposes a systematic and effective approach to analyze and predict the far-field CM radiation of a low-side Buck converter. The crucial findings of the current research scrutiny can also be of high benefit in analyzing, predicting, and suppressing the CM electromagnetic noise in other nonisolated power converters.

## REFERENCES


[1] O. Aouine, C. É. Labarre, and F. Ç. Costa, "Measurement and modeling of the magnetic near field radiated by a buck chopper," *IEEE Trans. Electromagn. Compat.*, vol. 50, no. 2, pp. 445–449, May 2008.

[2] H. Sun, L. Du, and G. Liang, "Calculation of electromagnetic radiation of VSC-HVDC converter system," *IEEE Trans. Magn.*, vol. 52, no. 3, Mar. 2016, Art. no. 9400504.

[3] M. Laour, R. Tahmi, and C. Vollaire, "Modeling and analysis of conducted and radiated emissions due to common mode current of a buck converter," *IEEE Trans. Electromagn. Compat.*, vol. 59, no. 4, pp. 1260–1267, Aug. 2017.

[4] H. Chen, T. Wang, L. Feng, and G. Chen, "Determining far-field EMI from near-field coupling of a power converter," *IEEE Trans. Power Electron.*, vol. 29, no. 10, pp. 5257–5264, Oct. 2014.

[5] Z. Ma, S. Wang, Q. Huang, and Y. Yang, "A review of radiated EMI research in power electronics systems," *IEEE J. Emerg. Sel. Topics Power Electron.*, vol. 12, no. 1, pp. 675–694, Feb. 2024.

[6] F. C. Lee, S. Wang, and Q. Li, "Next generation of power supplies—Design for manufacturability," *IEEE J. Emerg. Sel. Topics Power Electron.*, vol. 9, no. 6, pp. 6462–6475, Dec. 2021.

[7] Y. Zhang, S. Wang, and Y. Chu, "Analysis and comparison of the radiated electromagnetic interference generated by power converters with Si MOSFETS and GaN HEMTs," *IEEE Trans. Power Electron.*, vol. 35, no. 8, pp. 8050–8062, Aug. 2020.

[8] W. Kitagawa, T. Kutsuna, K. Kuwana, Y. Kawamura, and T. Takeshita, "Conducted noise simulation on ac–dc converter using SiC-MOSFET," *IEEE Trans. Ind. Appl.*, vol. 57, no. 2, pp. 1644–1651, Mar./Apr. 2021.

[9] D. M. Hockanson, J. L. Drewniak, T. H. Hubing, T. P. Van Doren, F. Sha, and M. J. Wilhelm, "Investigation of fundamental EMI source mechanisms driving common-mode radiation from printed circuit boards with attached cables," *IEEE Trans. Electromagn. Compat.*, vol. 38, no. 4, pp. 557–566, Nov. 1996.

[10] T. Watanabe, O. Wada, T. Miyashita, and R. Koga, "Common-mode current generation caused by difference of unbalance of transmission lines on a printed circuit board with narrow ground pattern," *IEICE Trans. Commun.*, vol. E83-B, no. 3, pp. 593–599, Mar. 2000.

[11] Y. Toyota, Y. Sakai, M. Torigoe, R. Koga, T. Watanabe, and O. Wada, "Fast and accurate estimation of radiated emission from printed circuit board using common-mode antenna model based on common-mode potential distribution," in *Proc. IEEE Int. Symp. Electromagn. Compat.*, Jul. 2007, vol. 2, pp. 702–707.

[12] N. Zhang, J. Kim, and S. Ryu, "Prediction of common-mode radiated emission of PCB with an attached cable using imbalance difference model," *IEICE Trans. Commun.*, vol. E98-B, no. 4, pp. 638–645, Apr. 2015.

[13] C. Su and T. H. Hubing, "Imbalance difference model for common-mode radiation from printed circuit boards," *IEEE Trans. Electromagn. Compat.*, vol. 53, no. 1, pp. 150–156, Feb. 2011.

[14] L. Niu and T. H. Hubing, "Rigorous derivation of imbalance difference theory for modeling radiated emission problems," *IEEE Trans. Electromagn. Compat.*, vol. 57, no. 5, pp. 1021–1026, Oct. 2015.

[15] J. Yao, S. Wang, and H. Zhao, "Measurement techniques of common mode currents, voltages, and impedances in a flyback converter for radiated EMI diagnosis," *IEEE Trans. Electromagn. Compat.*, vol. 61, no. 6, pp. 1997–2005, Dec. 2019.

[16] J. Yao, S. Wang, and Z. Luo, "Modeling, analysis, and reduction of radiated EMI due to the voltage across input and output cables in an automotive nonisolated power converter," *IEEE Trans. Power Electron.*, vol. 37, no. 5., pp. 5455–5465, May 2022.

[17] J. He, Z. Guo, and X. Li, "Mechanism model and prediction method of common mode radiation for a nonisolated very-high-frequency dc–dc converter with cables," *IEEE Trans. Power Electron.*, vol. 35, no. 10, pp. 10227–10237, Oct. 2020.

[18] J. He, H. Wang, P. Zhao, W. Wang, and L. Cao, "Common mode far field radiation mechanisms and prediction of a buck converter with cables based on common mode voltage mutation method," *IET power Electron.*, vol. 17, no. 12, pp. 1567–1582, Jan. 2024.

[19] M. Alkhatib, J. K. Breakall, U. L. Rohde, A. K. Poddar, and O. Alzaabi, "FEKO modeling for an alternative feed method for Arecibo Incoherent scatter radar," in *Proc. Int. Appl. Comput. Electromagnetics Soc. Symp.*, Mar. 2023, pp. 1–2, doi: 10.23919/ACES57841.2023.10114683.

[20] Y. Zhang, J. Wang, Z. Zhao, and J. Yang, "Numerical analysis of dielectric lens antennas using a ray-tracing method and HFSS software," *IEEE Antennas Propag. Mag.*, vol. 50, no. 4, pp. 94–101, Aug. 2008.

[21] A. P. Duffy, A. J. M. Martin, A. Orlandi, G. Antonini, T. M. Benson, and M. S. Woolfson, "Feature selective validation (FSV) for validation of computational electromagnetics (CEM). Part 1 – The FSV method," *IEEE Trans. Electromagn. Compat.*, vol. 48, no. 3, pp. 459–459, Aug. 2006.

[22] C. R. Paul, "The concept of dominant effect in EMC," *IEEE Trans. Electromagn. Compat.*, vol. 34, no. 3, pp. 363–367, Aug. 1992.


**Weixin Wang** received the B.S. degree in building electricity and intelligence and the M.S. degree in electrical engineering in 2019 and 2023, respectively, from the Harbin Institute of Technology, Harbin, China, where he is currently working toward the Ph.D. degree in electrical engineering.

His research interests include electromagnetic compatibility, power electronics, and its far-field radiation prediction.

**Junping He** (Senior Member, IEEE) received the bachelor's and master's degrees in electrical engineering from the Northern Jiaotong University, Beijing, China, in 1993 and 1999, respectively, and the Ph.D. degree in electrical engineering from Tsinghua University, Beijing, China, in 2003.

He researched as a Postdoctoral of Tsinghua University and Delta Power Electronics Center (DPEC), Shanghai, China, from 2003 to 2005. In 2005, he joined the Harbin Institute of Technology, Shenzhen, China, where he is currently an Associate Professor. He was a visiting Scholar with Electromagnetic Compatibility (EMC) Laboratory, Missouri University of Science and Technology, Rolla, MO, USA, from 2013 to 2014. His research interests include electromagnetic compatibility analysis and design in power electronics, renewable energy power generation, etc.

**Junhua Shu** received the B.S. degree in electrical engineering from Northeast Normal University, Changchun, China, in 2021, and the M.S. degree in electrical engineering from Harbin Institute of Technology, Shenzhen, China, in 2025.

He is currently working as an Engineer with China Southern Power Grid Shenzhen Power Supply Company, Shenzhen, China. Her research interests include electromagnetic compatibility, power electronics, and its modeling.

**Han Wang** received the bachelor's and master's degrees in electrical engineering from Harbin Institute of Technology, Harbin, China, in 2019, and 2022, respectively.

Her research interests include electromagnetic compatibility, power electronics, and their modeling. She is currently an Engineer of State Grid Nanjing Power Supply Company, Nanjing, China, mainly engaged in the electromagnetic modeling of electronics.

**Lingling Cao** received the bachelor's and master's degrees in electrical engineering from Nanjing University of Aeronautics and Astronautics, Nanjing, China, in 2008 and 2011, respectively, and the Ph.D. degree in electrical engineering from Hong Kong Polytechnic University, Hong Kong, China, in 2015.

She engaged in power electronics designs as a Postdoctoral with Hong Kong Polytechnic University, from 2016 to 2017. She joined the Harbin Institute of Technology (Shenzhen), Shenzhen city, China, where she is currently an Associate Professor. Her research interests include wireless power transfer technology, multiport power converter design, and electromagnetic compatibility design.